High-energy spin waves in the spin-1 square-lattice antiferromagnet La₂NiO₄

A. N. Petsch,[1,*] N. S. Headings,[1] D. Prabhakaran,[2] A. I. Kolesnikov ®,[3] C. D. Frost,[4] A. T. Boothroyd ®,[2] R. Coldea ®,[2] and S. M. Hayden ®[1,†]

[1]*H. H. Wills Physics Laboratory, University of Bristol, Bristol BS8 1TL, United Kingdom*
[2]*Department of Physics, University of Oxford, Clarendon Laboratory, Oxford OX1 3PU, United Kingdom*
[3]*Neutron Scattering Division, Oak Ridge National Laboratory, Oak Ridge, Tennessee 37831, USA*
[4]*ISIS Facility, Rutherford Appleton Laboratory, Chilton, Didcot OX11 0QX, United Kingdom*

Inelastic neutron scattering is used to study the magnetic excitations of the $S = 1$ square-lattice antiferromagnet La₂NiO₄. We find that the spin waves cannot be described by a simple classical (harmonic) Heisenberg model with only nearest-neighbor interactions. The spin-wave dispersion measured along the antiferromagnetic Brillouin-zone boundary shows a minimum energy at the $(1/2, 0)$ position as is observed in some $S = 1/2$ square-lattice antiferromagnets. Thus, our results suggest that the quantum dispersion renormalization effects or longer-range exchange interactions observed in cuprates and other $S = 1/2$ square-lattice antiferromagnets are also present in La₂NiO₄. We also find that the overall intensity of the spin-wave excitations is suppressed relative to linear spin-wave theory, indicating that covalency is important. Two-magnon scattering is also observed.

I. INTRODUCTION

Studies of quantum (low-spin) square-lattice antiferromagnets (SLAFMs) are motivated by the desire to understand the ground state and excitations of a model Heisenberg system, and because superconductivity can develop by doping $S = 1/2$ systems with antiferromagnetic interactions such as cuprates [1] and nickelates [2]. Large-S antiferromagnets (AFMs), such as Rb₂MnF₄ [3] ($S = 5/2$), are generally well described by the semiclassical, harmonic, linear spinwave theory (LSWT). In contrast, significant deviations from LSWT predictions have been observed in the spin excitations of $S = 1/2$ SLAFMs, such as La₂CuO₄ (LCO) [4,5] and copper deuteroformate tetradeuterate (CFTD) [6–8]. These systems show an anomaly in the excitations at the $(1/2,0)$ position, on the antiferromagnetic Brillouin zone (mBZ) boundary. The anomaly is characterized by a strongly suppressed one-magnon energy and spectral weight as well as a broadening of the response in energy ($\hbar\omega$) [5–11].

LCO [4,5] is a well-characterized $S = 1/2$ SLAFM based on transition-metal-oxide layers. It shows an unusual spin-wave dispersion which can be described with *ferromagnetic*

longer-range exchange interactions [second-nearest-neighbor (NN) interaction or cyclic exchange] rather than a renormalization of the dispersion by effects beyond the linear spin-wave approximation. In the Hubbard model, the longer-range exchange interactions result from the large t/U ratio [4]. Here we study the $S = 1$ system La₂NiO₄ (LNO) with smaller t/U ratio. This is a square-lattice 3d transition-metal-oxide antiferromagnet. Our aim is to determine whether the longer-range exchange interactions and $(1/2,0)$ or $(0,1/2)$ anomaly, respectively, observed in $S = 1/2$ systems, persist in other systems.

LNO shows three-dimensional (3D) magnetic order below $T_N \approx 320$ K with moderate spin-lattice coupling (the magnetic structure is discussed in Sec. II B). It is considered to be a Hubbard-Mott insulator in the Zaanen-Sawatzky-Allen scheme [12,13]. Above 75 K, LNO has the same *Bmab* "low-temperature orthorhombic" (LTO) structure as LCO. The magnitude of the ordered moments in La₂NiO₄ has been found to be reduced with respect to the $S = 1$ value. The moment reduction is believed to be due to a combination of covalency effects, arising from the antibonding orbitals of the Ni-O-Ni bonds [14–16], and zero-point spin fluctuations [17].

Previous inelastic neutron scattering (INS) [19,20] and resonant inelastic x-ray scattering (RIXS) [21] studies show the existence of spin waves up to ∼120 meV. A study [20] of the spin-wave dispersion in the (H, H, L) plane observed two distinct gapped modes corresponding to fluctuations in and out of the *ab* plane. The gaps were assigned to single-ion anisotropy. The Heisenberg NN interaction was determined to be $J \approx 30$ meV. No out-of-plane **c**-axis dispersion was observed, implying $J_\perp/J < 10^{-3}$ and making the magnetic excitations quasi-2D.

In this paper, we present time-of-flight (ToF) INS data collected throughout the entire Brillouin zone and up to energy

---

*apetsch@stanford.edu; Stanford Institute for Materials and Energy Sciences, Stanford University, Stanford, California 94305, USA; SLAC National Accelerator Laboratory, Menlo Park, California 94025, USA.

†s.hayden@bristol.ac.uk

transfers of $\hbar\omega \approx 170$ meV on a high-quality single crystal of LNO. This enables us to resolve an anomalous high-$\hbar\omega$ spin-wave dispersion which resembles behavior observed in the $S = 1/2$ SLAFM cuprate CFTD where it is assigned to quantum-dispersion-renormalization effects beyond linear-order spin-wave theory [6–8]. In addition, we show that the spectral weights are well described by a LSWT+1/S model if anisotropy, covalency effects, and two-magnon excitations are considered.

II. EXPERIMENTAL DETAILS

A LNO single crystal with a mass of 21.1 g was grown by the floating-zone technique and annealed at 1173 K in 5% CO and 95% CO_2 atmosphere to obtain the correct oxygen composition. A superconducting quantum interference device (SQUID) magnetometry measurement at 1 T shows a Néel temperature of $T_N(1\,\mathrm{T}) \approx 320$ K and a structural and spin reorientation transition at 75 K. Thus, the oxygen excess δ in La$_2$NiO$_{4+\delta}$ is $\delta < 0.007$ [18,22].

The ToF INS experiments were performed at the MAPS instrument at the ISIS Neutron and Muon Source at the Rutherford Appleton Laboratory [23,24] and the SEQUOIA instrument at the Spallation Neutron Source at the Oak Ridge National Laboratory [25]. Data were collected at $T = 10$ and $T = 6$ K, respectively. The sample was aligned with $(1\bar{1}0)$ vertically. All presented MAPS data are integrated over $L \in [-15, 15]$ r.l.u. and all presented SEQUOIA data are integrated over $L \in [-10, 10]$ r.l.u.

A. Crystallographic notation

The low-temperature structure of LNO is the low-temperature tetragonal (LTT) $P4_2/ncm$ structure [18]. This can be approximately described by the high-temperature tetragonal (HTT) $I4/mmm$ space group. We use the HTT conventional unit cell with $a = b = a_{\mathrm{HTT}} \approx 3.89$ Å and $c \approx 12.55$ Å to describe wave vectors in reciprocal space as $\mathbf{q} = H\mathbf{a}^\star + K\mathbf{b}^\star + L\mathbf{c}^\star \equiv (H, K, L)$ for the presentation of our data. For data integrated over L and the spin-wave theory, we abbreviate to a square-lattice 2D notation (H, K). For a square-lattice, the points (H, K) and (K, H) are equivalent.

B. Magnetic structure

At low temperatures, the host lattice of the antiferromagnetism in near stoichiometric LNO is believed to be $P4_2/ncm$ or LTT. Samples with a similar composition to ours develop a ferromagnetic (FM) component (i.e., show canting of the ordered moments) and have anomalies in the intensity of the antiferromagnetic Bragg peak measured by neutron scattering on entering the LTT state at $T \approx 75$ K [26]. Rodriguez-Carvajal *et al.* (Table 4) [18] show that only a magnetic structure belonging to the Γ_{3g} irreducible representation of the $P4_2/ncm$ space group is consistent with this. We therefore assume that there is spin reorientation on entering the $P4_2/ncm$ structure and the antiferromagnetic structure is described by this magnetic mode, as shown in Fig. 1. Note that this magnetic structure cannot be distinguished using diffraction from the Γ_{4g} representation of the $Bmab$ space group proposed by Ref. [18] if two domains, rotated by 90° around the **c** axis, of equal population are present. In the $P4_2/ncm$ space group,
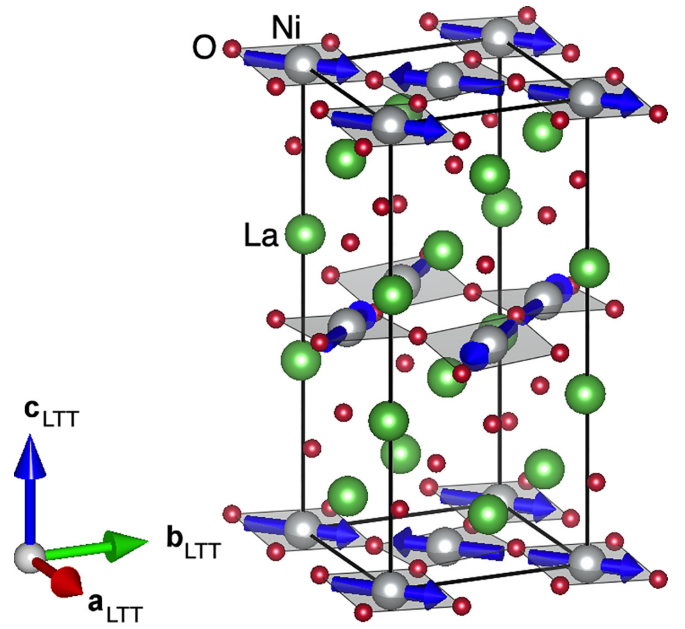

FIG. 1. The low-temperature crystal and magnetic structure of La$_2$NiO$_4$ based on Ref. [18]. Blue arrows denote the Ni spins. The unit cell in this figure is labeled with the $P4_2/ncm$ (LTT) space group with $a_{\mathrm{LTT}} = b_{\mathrm{LTT}} \approx 5.5$ Å and $c \approx 12.55$ Å. Shaded squares indicate the four planar-oxygen sites surrounding each Ni^{2+} ion and the buckling of the plane.

the local-point-group symmetry of the Ni^{2+} ions is $2/m$ and the moments are contained in the local mirror plane and point along the square diagonals of the LTT crystal structure such that the moments in adjacent layers are orthogonal, as shown in Fig. 1. In relation to the HTT structure, moments in the basal (middle) layer point almost along the **a** (**b**) direction in HTT notation.

III. RESULTS

The data are plotted and analyzed with the HORACE package [27]. Figure 2 shows representative slices through the data collected with an incident energy $E_i = 190$ meV at the SEQUOIA instrument in terms of the scattering law $S(\mathbf{q}, \omega) = \frac{k_i}{k_f} \frac{d^2\sigma}{d\Omega dE'}$. Data are normalized to absolute units via nuclear incoherent scattering from a vanadium standard, and are symmetrized about the $(H, H, 0)$, $(H, \overline{H}, 0)$, and $(H, 0, 0)$ lines. The data collected at the MAPS instrument appear very similar. The slices in Figs. 2(a)–2(d) show strong scattering as circles centered on $(3/2, 1/2)$, the center of an antiferromagnetic BZ. These are from one-magnon excitations, or spin waves. The scattering is consistent with spin gaps previously observed [20]. Around 92 meV, spin-wave branches dispersing from reciprocal lattice points [e.g., (200)] become observable near the corners. In Figs. 2(e) and 2(f), lines of scattering parallel to the magnetic BZ (mBZ) boundaries (dashed lines) are the spin-wave branches originating from the $(3/2, 1/2)$- and $(1, 0)$-type positions. The scattering in Figs. 2(g) and 2(h) is believed to be multimagnon excitations. At higher $\hbar\omega$, the spin waves appear stronger first at the corners of the mBZ, and then at highest $\hbar\omega$, at the midpoints
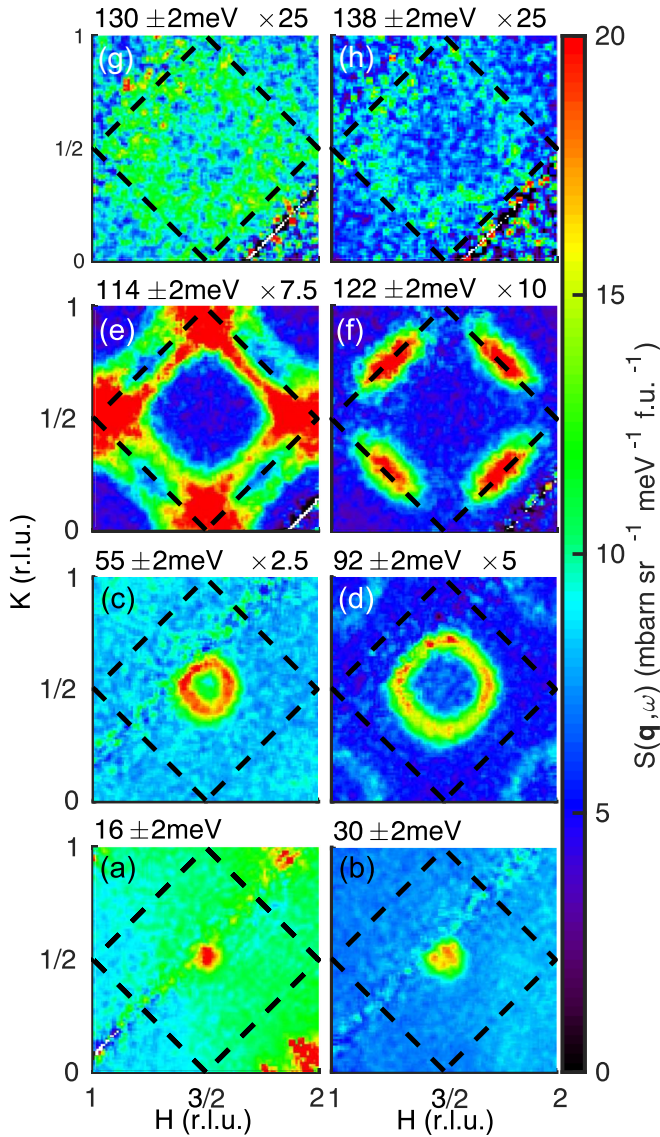
FIG. 2. Representative constant-$\hbar\omega$ slices through the LNO data collected on SEQUOIA with $E_i = 190$ meV. The circles and other structures in panels up to $\hbar\omega = 122$ meV are mostly due to single-magnon scattering. For $\hbar\omega \geqslant 130$ meV, two-magnon scattering is observed. The dashed lines are the mBZ boundaries.

FIG. 3. Magnetic excitations in La$_2$NiO$_4$. (a) Scattering function $S(\mathbf{q}, \omega)$ simulated from Eqs. (5)–(7) convoluted with finite life-time and resolution. (b) INS data collected with $E_i = 260$ meV at SEQUOIA. A background consisting of a smooth interpolation of a $\mathbf{q} = (1, 0)$ spectrum integrated over $L \in [-15, 15]$ has been subtracted from each $\mathbf{q}$. A nonlinear color-coded intensity scale is used to enhance the weak two-magnon scattering.

of the mBZ edges. This is unexpected for a classical NN Heisenberg SLAFM where no dispersion is expected along the mBZ boundaries. There, equal scattering, except for the magnetic form factor, is expected along the black dotted lines.

Our data are qualitatively consistent with a Néel SLAFM with single-ion anisotropy, significant multimagnon scattering, and an anomalous high-$\hbar\omega$ dispersion. For further analysis, a smooth function is fitted to a $\hbar\omega$-dependent cut at the *ferromagnetic* reciprocal-lattice position (1,0) and subtracted from all analyzed data. This removes most incoherent and multiphonon background.

The calculated and measured intensities of the magnetic excitations after background subtraction are shown in Figs. 3(a) and 3(b). The multimagnon scattering and anomalous dispersion are clearly visible at the mBZ boundary. The
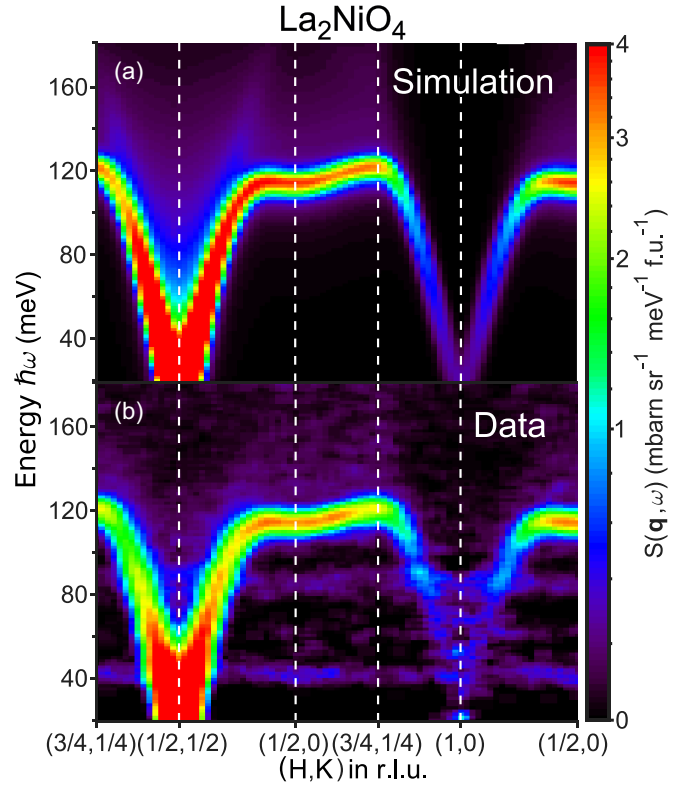
two, mostly dispersionless lines at $\sim$42 and $\sim$87 meV are optical phonon modes.

One-dimensional (1D) cuts are taken through the data along high-symmetry lines marked in the inset of Fig. 4(b) to fit the data with the model described in the following section. The data sets from both instruments are individually fitted to determine the model parameters. Some representative cuts with fits are shown in Fig. 4(d).

IV. SPIN-WAVE MODEL FOR A SINGLE NiO$_2$ PLANE

LNO is a Hubbard-Mott insulator; its magnetism is well described by an extended Heisenberg model with spin quantum number $S = 1$ on the Ni^{2+} ($3d^8$) sites with the orbital moments quenched by the octahedral-crystal-field environment of oxygen ions. We consider a single NiO$_2$ layer (the basal layer in Fig. 1) with the ordered moment along the **z** axis or **a** (see Sec. II A). The spin Hamiltonian can be written as [4,20,31–34]

$$
\begin{aligned}
\mathcal{H} = &\sum_{\langle i,j \rangle} J_{ij} \mathbf{S}_i \cdot \mathbf{S}_j + \sum_i \left[K_c \left(S_i^y\right)^2 + K_a \left(S_i^z\right)^2 \right] \\
&+ J^\square \sum_{\langle i,j,k,l \rangle} \left[(\mathbf{S}_i \cdot \mathbf{S}_j)(\mathbf{S}_k \cdot \mathbf{S}_l) + (\mathbf{S}_i \cdot \mathbf{S}_l)(\mathbf{S}_k \cdot \mathbf{S}_j) \right. \\
&\left. - (\mathbf{S}_i \cdot \mathbf{S}_k)(\mathbf{S}_j \cdot \mathbf{S}_l) \right],
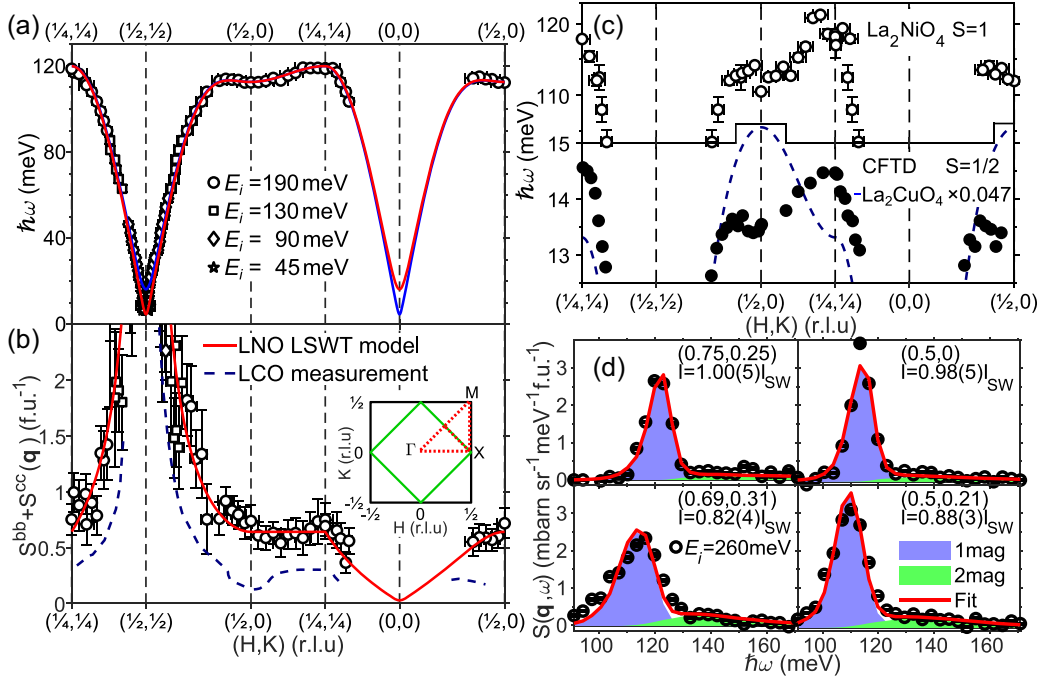\end{aligned} \tag{1}
$$

FIG. 4. Results of the data fitting and comparison with similar compounds. (a) Spin-wave dispersion (see Supplemental Material [28]) in red (blue) for the in-plane (out-of-plane) mode with the peak positions from the MAPS data. (b) Amplitude of the spin-wave pole in units of spin (multiply by $g^2\mu_B^2$ to get in units of μ_B^2) from the HORACE [27] fitting of Eqs. (5) and (6) to the MAPS data, LSWT prediction with $Z_{co} = 0.78(6)$ (red) and absolute results from LCO with $Z_{co} = 0.89(23)$ [5] for $Z_d(S = \frac{1}{2}) = 0.57$ [29,30] (blue dashed). (c) MAPS data in comparison with CFTD [6] and LCO dispersion scaled by $J(\text{CFTD})/Z_cJ(\text{LCO}) = 0.047$ [5] (blue dashed). It is noted that $(0, \frac{1}{2})$ is equivalent to $(\frac{1}{2}, 0)$. (d) Representative cuts through the SEQUOIA data fitted with the one+two-magnon model with $\hbar\Gamma = 1.5$ meV.

where J_{ij} represents the first- to third-NN Heisenberg exchange interactions J, J', and J'', $K_a \leqslant 0$ is an easy-axis anisotropy, and $K_c \geqslant 0$ is an out-of-plane hard-axis anisotropy. Here, (x, y, z) are along the HTT (b, c, a) axes, respectively (see Sec. II A). The local-anisotropy terms are symmetry allowed in the $2/m$ local-point-group symmetry of the Ni^{2+} ions in the LTT structure (the local mirror plane is ac) and are attributed to higher-order effects of the local crystal field and spin-orbit coupling. A bilinear-biquadratic interaction, suggested for $S = 1$, is neglected as it becomes indistinguishable from other interaction terms in the Néel state [35–37]. Also, an out-of-plane spin canting of 0.1°, assigned to a finite Dzyaloshinskii-Moriya interaction (DMI), has been observed [26]. Although DMI can induce nondegenerate spin-wave modes, the spin canting is too small to describe the previously reported gap size [20,26,38] (see Ref. [20] and Appendix D) and hence it is neglected in our analysis. The cyclic term $J^\square$ considered in LCO [39–42] is indistinguishable in LSWT from J' and is considered later (see, also, Appendix B).

The spin-wave excitations of the Hamiltonian are determined in the harmonic limit, commonly referred to as LSWT. For more details, see Appendices B and C. There are two distinct spin-wave modes for $K_c > 0$ corresponding to spin fluctuations along **b** (in plane) and **c** (out of plane), respectively. Their dispersion relations are given by $\hbar\omega_\mathbf{q}$ and $\hbar\omega'_\mathbf{q} = \hbar\omega_{\mathbf{q}+\boldsymbol{\tau}_{AF}}$, respectively, where

$$\hbar\omega_\mathbf{q} = Z_c\sqrt{A_\mathbf{q}^2 - B_\mathbf{q}^2}, \tag{2}$$

$$A_\mathbf{q} = 4S\left[-\frac{K_a}{2} + \frac{K_c}{4} + J - J'(1 - v_h v_k)\right], \tag{3}$$

$$B_\mathbf{q} = 4S\left[J\frac{v_h + v_k}{2} - \frac{K_c}{4}\right], \tag{4}$$

with $v_\xi = \cos(2\pi\xi)$ and $\boldsymbol{\tau}_{AF} = (1/2, 1/2)$ the Néel-magnetic-structure propagation vector, expressed in reciprocal-lattice units of the HTT unit cell. $Z_c \approx 1.09$ is a spin-fluctuation correction factor which renormalizes the excitation energy [17,43]. The Bogoliubov transformation parameters then yield the correlation (scattering) functions for the one- and two-magnon excitations in the $T \to 0$ limit [44–48] (see Appendix B),

$$S^{bb}(\mathbf{q}, \omega) = \frac{Z_d Z_{co} S}{2}|u_\mathbf{q} - v_\mathbf{q}|^2\delta(\hbar\omega - \hbar\omega_\mathbf{q}), \tag{5}$$

$$S^{cc}(\mathbf{q}, \omega) = \frac{Z_d Z_{co} S}{2}|u_{\mathbf{q}+\boldsymbol{\tau}_{AF}} + v_{\mathbf{q}+\boldsymbol{\tau}_{AF}}|^2\delta(\hbar\omega - \hbar\omega_{\mathbf{q}+\boldsymbol{\tau}_{AF}}), \tag{6}$$

$$S^{aa}(\mathbf{q}, \omega) = NZ_{co}^2(S - \Delta S)^2\delta(\hbar\omega)\delta(\mathbf{q} - \boldsymbol{\tau}_{AF} - \boldsymbol{\tau})$$
$$+ \frac{Z_{2M}Z_{co}}{2N}\sum_{\mathbf{q}_1,\mathbf{q}_2} f(\mathbf{q}_1, \mathbf{q}_2)\delta(\hbar\omega - \hbar\omega_{\mathbf{q}_1} - \hbar\omega_{\mathbf{q}_2})$$
$$\times \delta(\mathbf{q} - \boldsymbol{\tau}_{AF} - \mathbf{q}_1 - \mathbf{q}_2 - \boldsymbol{\tau}), \tag{7}$$

where $u_\mathbf{q} = \cosh\theta_\mathbf{q}$, $v_\mathbf{q} = \sinh\theta_\mathbf{q}$, and $\tanh(2\theta_\mathbf{q}) = B_\mathbf{q}/A_\mathbf{q}$, $f(\mathbf{q}_1, \mathbf{q}_2) = |u_{\mathbf{q}_1}v_{\mathbf{q}_2} + u_{\mathbf{q}_2}v_{\mathbf{q}_1}|^2$. N is the total number of spins in the lattice, $\boldsymbol{\tau}$ is a (HTT structural) reciprocal-lattice vector, and $\Delta S = \langle v^2\rangle$ is the zero-point spin reduction, where

⟨·⟩ means the average over the full Brillouin zone. The first term in S^{aa} (denoting fluctuations along the **a** axis) contains the elastic magnetic Bragg peak and the second term is the inelastic two-magnon continuum, with one of the two wave vectors in the sum restricted to one full Brillouin zone. The above dynamical correlations and the dispersion relation $\omega_\mathbf{q}$ have the translational periodicity of the full Brillouin zone.

The prefactor Z_d is a one-magnon intensity renormalization factor due to higher-order effects neglected at linear order in spin-wave theory; Z_{2M} is a corresponding factor for the two-magnon scattering. We have also included an additional factor Z_{co} in Eqs. (5)–(7) to take account of covalency effects, $Z_{co} = 1$ in the absence of these. For $K_c = 0$, $Z_d = 1 - \Delta S/S$, and assuming $Z_{2M} = 1$, the total-spin sum rule is satisfied such that elastic, one-magnon and two-magnon scattering integrated over all energies and a full Brillouin zone add up to $S(S+1)$ per spin, shared between the three contributions as $(S - \Delta S)^2$, $(S - \Delta S)(2\Delta S + 1)$, and $\Delta S(\Delta S + 1)$, respectively. To derive the above, we have used the fact that u is even and v is odd with respect to a wave-vector shift by the magnetic propagation vector $\boldsymbol{\tau}_{AF}$, so the average $\langle uv \rangle = 0$. For finite K_c, this is no longer the case and, to satisfy the total sum rule, one needs to use

$$Z_d = 1 - \frac{\Delta S}{S} - \frac{\langle uv \rangle^2}{S(2\Delta S + 1)} \qquad (8)$$

as the integrated two-magnon scattering becomes $\Delta S(\Delta S + 1) + \langle uv \rangle^2$.

Significant two-magnon scattering is observed even in spin-5/2 systems. So we expect to also see this in the present $S = 1$ system [3] and signatures are presented in Fig. 4(d) and Figs. 2(g) and 2(h), as shown in Figs. 5(b) and 5(c), respectively. Equation (7) is evaluated on a three-dimensional grid $(\mathbf{q}_{2D}, \hbar\omega)$ and then convolved with a **q**-independent inverse lifetime of $\hbar\Gamma = 1.5$ meV per excited magnon. To fit the data, Eqs. (5) and (6) are added after lifetime broadening to the three-dimensional grid and these spin-spin correlation functions are then multiplied by the anisotropic magnetic form factor of the Ni^{2+} e_g orbitals [49–53]. Deviations due to covalency are included through the factor Z_{co}. Finally, these functions are convolved with the instrument resolution function by TOBYFIT in the HORACE package [27]. Simulations of $S^{aa}(\mathbf{q}, \omega)$ without instrumental and lifetime broadening are shown in Fig. 5. The two-magnon term appears unusual due to the anisotropy gaps resulting in a "peak" above $\hbar\omega_\mathbf{q}$, rather than a tail arising at $\hbar\omega_\mathbf{q}$. It is further observed that the instrument resolution dominates the broadening.

V. DISPERSION

In order to plot the dispersion, we fitted Gaussian functions to 1D cuts through the data to obtain the peak positions, plotted in Fig. 4(a). Constant-**q** cuts with $E_i = 45$ meV at low $\hbar\omega$ clearly show two distinct gapped spin-wave modes (not shown). The high-$\hbar\omega$ excitations show dispersion along the mBZ boundary. From the lower-$\hbar\omega$ data ($\leqslant 50$ meV), we can obtain an estimate of the $J \approx 29$ meV and the spin gaps at (1/2,1/2), $\Delta_1 \approx 4Z_c\sqrt{J(-K_a)} \approx 5$ meV and $\Delta_2 \approx 4Z_c\sqrt{J(K_c - K_a)} \approx 16$ meV, are in good agreement with
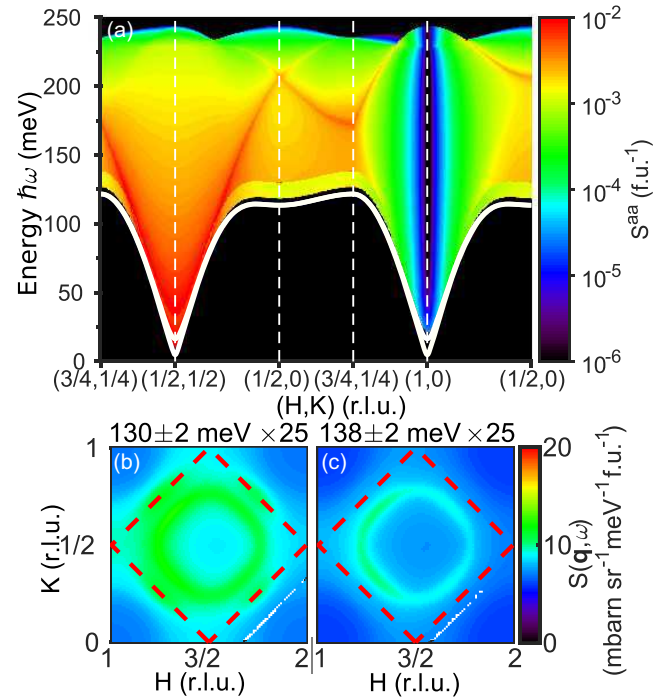

FIG. 5. (a) Simulation of two-magnon scattering using Eq. (7). The solid white lines show the magnon dispersions $\hbar\omega_\mathbf{q}$ and $\hbar\omega_{\mathbf{q}+\boldsymbol{\tau}_{AF}}$. (b),(c) Simulations of $S(\mathbf{q}, \omega)$ due to two-magnon scattering with an added constant background of 0.28 or 0.24 mb^{-1} sr^{-1} f.u.$^{-1}$, respectively. These closely resemble the slices in Figs. 2(g) and 2(h), respectively.

previous work [20]. We mostly fixed K_a (see Table I) when fitting the whole dispersion curve below.

The high-$\hbar\omega$ dispersion cannot be described by J only in LSWT, but requires a finite J'. The upturn from $\mathbf{q} = (1/2, 0)$ to $\mathbf{q} = (1/4, 1/4)$ can be described by an antiferromagnetic $J' > 0$, with $J' \approx 5.8(3)\%$ of J which yields, including the anisotropy, a difference of $\sim 6\%$ between $(1/2, 0)$ and $(1/4, 1/4)$. The $J' > 0$ describes the dispersion along the mBZ boundaries, as well as the local dispersion minimum at $(1/2, 0)$. Adding J'', described in Eq. (B2), does not improve the fitting and is hence neglected from now on.

TABLE I. Fitted Heisenberg coupling and anisotropy constants which determine the dispersion given in Eq. (2). The rows describe different fitting models: the first row includes no J'', the second row includes all terms but with K_a fixed and adapted from Ref. [20], and the third row excludes J'' and again uses the value from Ref. [20] for K_a. The fourth row parameterizes the second row in terms of J and $J^\square$. Parameters marked (−) are fixed during fitting.

J (meV)	J' (meV)	J'' (meV)	$J^\square$ (meV)	K_a (meV)	K_c (meV)
29.02(8)	1.68(5)	0 (−)	0 (−)	−0.035(3)	0.443(11)
28.2(11)	1.3(5)	−0.2(3)	0 (−)	−0.04 (−)	0.46(2)
29.00(8)	1.67(5)	0 (−)	0 (−)	−0.04 (−)	0.445(11)
32.34(13)	0 (−)	0 (−)	−1.67(5)	−0.04 (−)	0.445(11)

TABLE II. Comparison of exchange constants for square-lattice 3D transition-metal-oxide AFMs. Here, S is the spin and t/U indicates results from fitting with the extended t/U expansion [39–41,54].

	S	J (meV)	J' (meV)	J'' (meV)	$J^\square$ (meV)
La$_2$CuO$_4$ [5]	1/2	114(2)	−12(2)	2.9(2)	0(−)
La$_2$CuO$_4$, t/U [5]	1/2	143(2)	2.9(2)	2.9(2)	58(4)
La$_2$NiO$_4$	1	28.2(11)	1.3(5)	−0.2(3)	0(−)
La$_2$CoO$_4$ [55]	3/2	9.69(2)	0.43(1)	0.12(2)	0(−)

La$_2$CuO$_4$ shows an inverted dispersion (with respect to LNO) along the mBZ boundary $[(0, 1/2) - (1/4, 1/4)]$ and $J' < 0$ (when $J^\square = 0$) [4] [see Fig. 4(c)]. The dispersion in LCO can be explained by higher-order terms in the t/U expansion of the Hubbard model for hopping between Cu sites. This yields terms in $J^\square$, J', and J'' [39–41,54]. The term in $J^\square$ has the same effect on the dispersion as J' in LSWT [see Eq. (B2)] so cannot be distinguished from J'.

The $S = 3/2$ $3d$ square-lattice transition-metal-oxide AFM La$_2$CoO$_4$ (LCoO) has the same LTT structure as La$_2$NiO$_4$ and neutron scattering measurements of the magnon dispersion have also been carried out on this material [55]. The spin-wave excitations in LCoO also show dispersion along the mBZ with a minimum at $(1/2, 0)$, as in LNO, but the effect is weaker in LCoO than in LNO. In Table II, we compare the exchange couplings of LCO, LNO, and LCoO. Both LNO and LCoO have $J' > 0$. Thus, the anomalous compound is LCO, which yields $J' < 0$ when fitted with $J^\square = 0$. The natural conclusion is that cyclic exchange is present in LCO, but negligible in LNO and LCoO, which is consistent with the more substantial t/U in LCO.

As shown in Fig. 4(c) the high-$\hbar\omega$ dispersion in LNO, however, closely resembles the dispersion in the $S = 1/2$ SLAFM copper deuteroformate tetradeuterate (CFTD) [6–8] as well as similar compounds such as Cu(pyrazine)$_2$ (ClO$_4$)$_2$ [9,10] and CuF$_2$(H$_2$O)$_2$ (pyrazine) [11]. In these compounds, the dispersion along the mBZ is explained by quantum effects which renormalize the dispersion. The dispersion in $S = 1/2$ SLAFMs is predicted by various theoretical calculations. Although all models predict a dispersion on the mBZ boundary, they disagree over the magnitude of the dispersion and its origin. To our knowledge, no calculations are available at the time of the submission for $S = 1$ SLAFMs, but from the Holstein-Primakoff transformation, a suppression of quantum effects by at least a factor of two from $S = 1/2$ to $S = 1$ systems is predicted [56].

VI. SPECTRAL WEIGHT

The 1D cuts, taken from the MAPS instrument data, are used to fit the overall spectral weights due to the better resolution at low $\hbar\omega$. The cuts are fitted with the intensities calculated from Eqs. (5) and (6) convolved with a **q**-independent inverse lifetime Γ. A linear function is added to remove multimagnon scattering and a **q**-dependent background. The fitted one-magnon spectral weights throughout the lattice BZ are depicted in Fig. 4(b). The **q** dependence

of the one-magnon spectral weights is qualitatively well described by the LSWT model. Small deviations arise near the antiferromagnetic BZ center; first, because the anisotropy prevents the divergence of the spectral weight there, and second, the fitting is hindered by contamination from the magnetic Bragg peak and the multimagnon scattering. Utilizing the Hamiltonian parameters determined from the dispersion relations, we find $\Delta S = 0.188(1)$ and $\langle uv \rangle = -0.017(1)$, yielding $Z_d \approx 0.812(1)$. For a fit of the high-$\hbar\omega$ one-magnon excitations using Eqs. (5)–(7), with $Z_d \approx 0.812(1)$, the SEQUOIA data yield $Z_{co} = 0.78(6)$. The Z_d follows from $\Delta S = 0.188(1)$ and $\langle uv \rangle = -0.017(1)$, therein derived from the Hamiltonian parameters of the fitted dispersion relation. We believe $Z_{co} < 1$ because there is a reduction of the ordered Ni^{2+} moment due to oxygen covalency effects, as observed in neutron diffraction [14–16].

In the related spin-1/2 compounds LCO and CFTD, anomalous scattering is observed near the $(1/2,0)$ and equivalent $(0,1/2)$ point. To study if such scattering also arises in LNO, the one+two-magnon model is fitted to 59 constant-**q** cuts through the high-$\hbar\omega$ excitations in the SEQUOIA data. The model includes Z_{co} and the subsequent analysis focuses particularly on the comparison of $(1/4,1/4)$ and the anomalous $(1/2,0)$ point. All cuts are fitted with a small individual constant background term to account for **q**-dependent variations in the background. Some representative fits are shown in Fig. 4(d), where $\Gamma = 1.5$ meV and the fits are unchanged for smaller Γ values.

As shown in Fig. 4(d), the model gives a good description of peak shapes and continua and, further, of the relative intensities of one- and two-magnon spectral weights. The calculated spectral weights also agree quantitatively well with the measured spectral weights after rescaling for Z_{co}. Moreover, the model including Z_{co} gives a good description along all high-symmetry directions, as shown in Figs. 3(a) and 3(b).

In contrast to the $S = 1/2$ compounds CFTD [6–8] and LCO [5], in LNO neither the reduced one-magnon spectral weight [see Fig. 4(b)] nor the enhanced multimagnon spectral weight is observed at $(1/2,0)$ within the statistical limitations.

VII. DISCUSSION

In the preceding sections, we have seen that although aspects of the magnetic excitations of LNO are qualitatively described by a simple linear spin-wave theory with two-magnon scattering, the intensity and dispersion show some significant deviations. The measured spin-wave dispersion is well described by an anisotropic semiclassical NN Heisenberg AFM below ∼100 meV. This theory also qualitatively describes the two-magnon excitations observed for $\hbar\omega \approx 130$ meV. Two aspects of the excitations that are not well described by LSWT are the overall intensity of the excitations and the dispersion of the high-$\hbar\omega$ excitations.

The overall intensity of the excitations is determined by the absolute normalization of the measured signal and yields a scaling factor of $Z_{co} = 0.78(6)$ through Eqs. (5) and (6) when the quantum renormalization factor Z_d is taken into account. The most likely explanation for the difference from $Z_{co} = 1$ is the covalency effects [14–16] present in nickel oxides. This results in some of the ordered and fluctuating magnetic

moments residing on the oxygen atoms, reducing the signal seen in the present experiment.

We also observe a deviation from the predictions of LSWT for a NN SLAFM in the form of significant dispersion along the mBZ boundaries. The dispersion indicates the presence of longer-range exchange interactions. The structurally related compound LCO also shows dispersion along the mBZ boundaries, but with the opposite sense [4]. In the case of LCO, the dispersion is due to the substantial $t/U \approx 0.11$, resulting in a substantial *ferromagnetic* next-NN exchange $J' < 0$ in superexchange theory [39–41,54]. Such a mechanism cannot explain the *antiferromagnetic* $J' > 0$ observed in LNO and LCoO. An anisotropy in J as the origin of the high-$\hbar\omega$ dispersion is also excluded, as this would imply two distinct high-$\hbar\omega$ spin-wave modes with differing dispersion, as shown in Ref. [57].

Thus, our observation of a downward dispersion from $(1/4,1/4)$ to $(1/2,0)$ seems to have two possible explanations. Either further-NN superexchange in La_2NiO_4 yields an antiferromagnetic J' or the quantum renormalization of the spin-wave dispersion proposed for the $S = 1/2$ NN SLAFMs [6–11] is also present in $S = 1$ systems. Testing the first proposal will require detailed electronic structure calculations of the next-NN superexchange in La_2NiO_4. This is beyond the scope of this present study. However, we note that t/U is smaller in La_2NiO_4 and that other pathways such as Ni-O-O-Ni with direct overlap between the oxygens may be more important in La_2NiO_4 than La_2CuO_4 [58]. Thus, the t' hopping involving these oxygens could yield an antiferromagnetic J'.

A second proposal, that the downward dispersion is due to a renormalization of the spin-wave energies, is supported by the similarity to $S = 1/2$ SLAFMs: CFTD [6–8], $Cu(pyrazine)_2$ $(ClO_4)_2$ [9,10], and $CuF_2(H_2O)_2$ (pyrazine) [11]. Furthermore, it resembles the dispersion predicted by various theoretical models for $S = 1/2$ NN SLAFMs. These models suggest that quantum effects lead to an anomaly in the dispersion at $(1/2,0)$. The techniques used in the models are series expansions (SEs) of the NN Heisenberg-Ising model [59,60], quantum Monte Carlo simulations [61,62], exact diagonalization [63], continuous similarity transformations [64,65], and density matrix renormalization group (DMRG) simulations [56].

In CFTD [6–8] and LCO [5], the one-magnon spectral weight is suppressed near $(1/2,0)$ relative to LSWT and a strong continuum with longitudinal and transverse character is observed. LSWT predicts the same one-magnon spectral weight along the entire mBZ boundary. However, some of the other models for $S = 1/2$ quantum SLAFM mentioned above predict the suppressed spectral weight and continuum near $(1/2, 0)$. We find no evidence for a wave-vector-dependent variation of the one-magnon spectral weight or continuum at $(1/2,0)$ in LNO.

VIII. CONCLUSION

Our results show that magnetic excitations in La_2NiO_4 are not described by a simple classical ($S \to \infty$) Heisenberg model with only nearest-neighbor interactions. The energy of the spin waves disperses along the antiferromagnetic

Brillouin zone boundary from $(1/4,1/4)$ to a minimum at $(1/2,0)$. This is in the opposite sense to that in the $S = 1/2$ system La_2CuO_4, but the same sense as in other $S = 1/2$ systems with smaller t/U and the isostructural $S = 3/2$ compound La_2CoO_4. The origin of the dispersion in La_2NiO_4 is unclear. It may be due to a quantum renormalization of the spin-wave energies or an antiferromagnetic second-nearest-neighbor superexchange. The overall intensity of the spin-wave excitations is suppressed relative to linear spin-wave theory, probably due to covalency effects.

APPENDIX A: NEUTRON SCATTERING AND DYNAMIC CORRELATION FUNCTIONS

Inelastic neutron scattering measures dynamic spin-spin correlation functions defined as

$$S^{\alpha\beta}(\mathbf{q}, \omega) = \frac{1}{2\pi\hbar} \int_{-\infty}^{\infty} e^{-i\omega t} \langle S_{\mathbf{q}}^{\alpha}(0) S_{-\mathbf{q}}^{\beta}(t) \rangle \, dt, \qquad (A1)$$

where $\mathbf{S_q}$ is the Fourier-transformed spin operator [34,66] (multiply by $g^2\mu_B^2$ to get in units of μ_B^2). Our model spin-wave calculations compute $S^{\alpha\beta}(\mathbf{q}, \omega)$, which is diagonal in our case. In the dipole approximation, the magnetic inelastic neutron scattering cross section is given by

$$\frac{d^2\sigma}{d\Omega dE'} = \frac{k_f}{k_i} S(\mathbf{q}, \omega)$$

$$= \frac{k_f}{k_i} \left(\frac{\gamma r_e}{2\mu_B} \right)^2 |F(\mathbf{q})|^2 e^{-2W}$$

$$\times \sum_{\alpha\beta} \left(\delta_{\alpha\beta} - \frac{q_\alpha q_\beta}{q^2} \right) g^2 \mu_B^2 S^{\alpha\beta}(\mathbf{q}, \omega), \quad (A2)$$

where $g \approx 2$, $e^{-2W} \approx 1$ for low temperatures, $F(\mathbf{q})$ is the magnetic form factor, μ_B is the Bohr magneton, and $(\gamma r_e/2)^2 = 72.4$ mb.

While the model is derived for the basal NiO_2 layer in Fig. 1 with the spins aligned along the HTT **a** axis, S^{aa} and S^{bb} for neighboring NiO_2 planes in the LTT structure are related by a $90°$ rotation around **c**. This implies that in successive

planes, the fluctuations along the HTT **a** and **b** axes are interchanged. In the analysis, this is considered by averaging the polarization factor over both axes.

Furthermore, although $S(\mathbf{q}, \omega)$ is averaged over a range in L by utilizing the HORACE [27] package, the **q** vectors of the averaged pixels (neutrons) are retained and are then included in the calculations of Eq. (A2). It is then averaged over the calculated values of $S(\mathbf{q}, \omega)$. This accounts for the **q** dependence of the polarization factor and the magnetic form factor. For more details, see Ref. [27] and HORACE documentation.

APPENDIX B: DERIVATION OF CORRELATION FUNCTIONS USING ROTATING REFERENCE FRAME

Here we summarize the derivations of the dynamical correlations (included two-magnon correlations) within linear spin-wave theory for a square-lattice spin Hamiltonian appropriate for the $S = 1$ Ni^{2+} layers in La$_2$NiO$_4$, as given in Eq. (1) with a collinear two-sublattice Néel magnetic structure.

It is convenient to transform the Hamiltonian to a rotating reference frame [48] where the local xyz spin axes at every site are defined such that **z** is along the local ordered spin direction. In this frame, the ground state is ferromagnetic and the magnetic unit cell is the same as the structural primitive unit cell (one spin per cell). This can be achieved by labeling the spin axes on the Néel A sublattice (which contains the origin) with ordered spins along the $+a$ axis as (x, y, z) along (b, c, a) and for the B sublattice with spins along $-a$ as (x, y, z) along $(b, -c, -a)$, so that at a general site **r**, the spin components are given by $S_{\mathbf{r}}^x = S_{\mathbf{r}}^b$, $S_{\mathbf{r}}^y = -S_{\mathbf{r}}^a \sin(\boldsymbol{\tau}_{AF} \cdot \mathbf{r}) + S_{\mathbf{r}}^c \cos(\boldsymbol{\tau}_{AF} \cdot \mathbf{r})$ and $S_{\mathbf{r}}^z = S_{\mathbf{r}}^a \cos(\boldsymbol{\tau}_{AF} \cdot \mathbf{r}) + S_{\mathbf{r}}^c \sin(\boldsymbol{\tau}_{AF} \cdot \mathbf{r})$ with $\boldsymbol{\tau}_{AF} = (1/2, 1/2)$ the Néel magnetic structure propagation vector, expressed in reciprocal lattice units of the structural HTT cell. Here, $(S_{\mathbf{r}}^a, S_{\mathbf{r}}^b, S_{\mathbf{r}}^c)$ are the spin components along the crystallographic HTT axes. In the rotating frame, the spin-wave Hamiltonian to quadratic order is obtained as

$$\mathcal{H}_{\rm rot} = \frac{1}{2} \sum_{\mathbf{q}} [a_{\mathbf{q}}^{\dagger} \quad a_{-\mathbf{q}}] \begin{bmatrix} A_{\mathbf{q}} & B_{\mathbf{q}} \\ B_{\mathbf{q}} & A_{\mathbf{q}} \end{bmatrix} \begin{bmatrix} a_{\mathbf{q}} \\ a_{-\mathbf{q}}^{\dagger} \end{bmatrix}, \qquad \text{(B1)}$$

where the sum extends over all wave vectors **q** in the full (structural) Brillouin zone and $a_{\mathbf{q}}^{\dagger}$ is the Fourier-transformed spin creation operator. Here (including the cyclic exchange), we have

$$A_{\mathbf{q}} = 4S \left[-\frac{K_a}{2} + \frac{K_c}{4} + (J - 2S^2 J^{\square}) \right.$$
$$\left. - (J' - S^2 J^{\square})(1 - v_h v_k) - J''(2 - v_h^2 - v_k^2) \right],$$

$$B_{\mathbf{q}} = 4S \left[(J - 2S^2 J^{\square}) \left(\frac{v_h + v_k}{2} \right) - \frac{K_c}{4} \right], \qquad \text{(B2)}$$

with $v_{\xi} = \cos(2\pi\xi)$. The 2×2 Hamiltonian matrix in Eq. (B1) can be brought to diagonal form using a Bogoliubov basis transformation,

$$\begin{bmatrix} a_{\mathbf{q}} \\ a_{-\mathbf{q}}^{\dagger} \end{bmatrix} = \begin{bmatrix} u_{\mathbf{q}} & -v_{\mathbf{q}} \\ -v_{\mathbf{q}} & u_{\mathbf{q}} \end{bmatrix} \begin{bmatrix} \alpha_{\mathbf{q}} \\ \alpha_{-\mathbf{q}}^{\dagger} \end{bmatrix}, \qquad \text{(B3)}$$

where $\alpha_{\mathbf{q}}^{\dagger}$ creates a spin wave with dispersion $\hbar\omega_{\mathbf{q}} = Z_c \sqrt{A_{\mathbf{q}}^2 - B_{\mathbf{q}}^2}$, $u_{\mathbf{q}} = \cosh\theta_{\mathbf{q}}$, $v_{\mathbf{q}} = \sinh\theta_{\mathbf{q}}$, and $\tanh(2\theta_{\mathbf{q}}) = B_{\mathbf{q}}/A_{\mathbf{q}}$. Here, Z_c is a dispersion renormalization factor due to higher-order effects neglected at linear order in spin-wave theory. The dynamical correlations in the rotating frame (at zero temperature) are obtained as

$$S^{xx}(\mathbf{q}, \omega) = Z_d \frac{S}{2} |u_{\mathbf{q}} - v_{\mathbf{q}}|^2 \delta(\hbar\omega - \hbar\omega_{\mathbf{q}})$$
$$= Z_d \frac{S}{2} \sqrt{\frac{A_{\mathbf{q}} - B_{\mathbf{q}}}{A_{\mathbf{q}} + B_{\mathbf{q}}}} \delta(\hbar\omega - \hbar\omega_{\mathbf{q}}), \qquad \text{(B4)}$$

$$S^{yy}(\mathbf{q}, \omega) = Z_d \frac{S}{2} |u_{\mathbf{q}} + v_{\mathbf{q}}|^2 \delta(\hbar\omega - \hbar\omega_{\mathbf{q}})$$
$$= Z_d \frac{S}{2} \sqrt{\frac{A_{\mathbf{q}} + B_{\mathbf{q}}}{A_{\mathbf{q}} - B_{\mathbf{q}}}} \delta(\hbar\omega - \hbar\omega_{\mathbf{q}}), \qquad \text{(B5)}$$

$$S^{zz}(\mathbf{q}, \omega) = N(S - \Delta S)^2 \delta(\hbar\omega)\delta(\mathbf{q} - \boldsymbol{\tau})$$
$$+ \frac{Z_{2M}}{2N} \sum_{\mathbf{q}_1, \mathbf{q}_2} f(\mathbf{q}_1, \mathbf{q}_2)\delta(\hbar\omega - \hbar\omega_{\mathbf{q}_1} - \hbar\omega_{\mathbf{q}_2})$$
$$\times \delta(\mathbf{q} - \mathbf{q}_1 - \mathbf{q}_2 - \boldsymbol{\tau}). \qquad \text{(B6)}$$

The dynamical correlations in the original (fixed) reference frame [Eqs. (5)–(7)] are obtained through Fourier transformation, such that $S^{bb} \equiv S^{xx}$, whereas $S^{aa}(\mathbf{q}, \omega) = S^{zz}(\mathbf{q} + \boldsymbol{\tau}_{AF}, \omega)$ and $S^{cc}(\mathbf{q}, \omega) = S^{yy}(\mathbf{q} + \boldsymbol{\tau}_{AF}, \omega)$, i.e., the latter two correlation functions are momentum shifted by $\boldsymbol{\tau}_{AF}$. In obtaining Eqs. (5)–(7), we have used the fact that $2\boldsymbol{\tau}_{AF}$ is a vector of the reciprocal lattice of the HTT structural cell, so wave vectors $\mathbf{q} - \boldsymbol{\tau}_{AF}$ and $\mathbf{q} + \boldsymbol{\tau}_{AF}$ are equivalent by reciprocal-space translational symmetry.

The in-plane (along **b**) spin correlations shows a magnon mode with dispersion $\omega_{\mathbf{q}}$ [red line in Fig. 4(a)] with the gap

$$\Delta_1 = 4Z_c S \sqrt{\left(2J - \frac{K_a}{2} + \frac{K_c}{2}\right)\frac{-K_a}{2}}$$
$$\approx 4Z_c S \sqrt{J(-K_a)}, \qquad \text{(B7)}$$

and strong intensity above the antiferromagnetic Bragg peaks at $\boldsymbol{\tau} + \boldsymbol{\tau}_{AF}$, and the larger gap

$$\Delta_2 = 4S \sqrt{\left(2J - \frac{K_a}{2}\right)\left(\frac{-K_a}{2} + \frac{K_c}{2}\right)}$$
$$\approx 4Z_c S \sqrt{J(K_c - K_a)}, \qquad \text{(B8)}$$

and weak intensity at $\boldsymbol{\tau}$. The out-of-plane correlations (along **c**) will show the wave-vector-shifted dispersion $\omega_{\mathbf{q}}' = \omega_{\mathbf{q}+\boldsymbol{\tau}_{AF}}$ [blue line in Fig. 4(a)] with reversed gaps compared to $\omega_{\mathbf{q}}$, i.e., gap Δ_1 at $\boldsymbol{\tau}$ and Δ_2 at $\boldsymbol{\tau} + \boldsymbol{\tau}_{AF}$. The longitudinal correlations (along a) will show the elastic magnetic Bragg peaks at $\boldsymbol{\tau} + \boldsymbol{\tau}_{AF}$ and a two-magnon continuum, with a gap of $\Delta_1 + \Delta_2$ at $\boldsymbol{\tau}$ and onsets with gaps at $2\Delta_1$ and $2\Delta_2$ at $\boldsymbol{\tau} + \boldsymbol{\tau}_{AF}$.

APPENDIX C: DERIVATION OF CORRELATION FUNCTIONS USING ANTIFERROMAGNETIC UNIT CELL

The dynamical correlation functions, derived in Appendix B, can also be derived in the antiferromagnetic unit

cell. Utilizing this unit cell implies a doubling of the number of Ni^{2+} ions per unit cell, and thus an effective doubling of the spin-wave modes, but does not require the transformation of the Hamiltonian to a rotating reference frame. The notations used in this section are the same as in Appendix B.

For the antiferromagnetic unit cell, the spin-wave Hamiltonian to quadratic order can be written as

$$\mathcal{H} = \frac{1}{2}\sum_{\mathbf{q}}\begin{bmatrix} a_{\mathbf{q}}^{\dagger} \\ b_{\mathbf{q}} \\ a_{-\mathbf{q}} \\ b_{-\mathbf{q}}^{\dagger} \end{bmatrix}^{T}\begin{bmatrix} A_{\mathbf{q}} & B_{\mathbf{q}}' & -SK_c & 0 \\ B_{\mathbf{q}}' & A_{\mathbf{q}} & 0 & -SK_c \\ -SK_c & 0 & A_{\mathbf{q}} & B_{\mathbf{q}}' \\ 0 & -SK_c & B_{\mathbf{q}}' & A_{\mathbf{q}} \end{bmatrix}$$

$$\times \begin{bmatrix} a_{\mathbf{q}} \\ b_{\mathbf{q}}^{\dagger} \\ a_{-\mathbf{q}}^{\dagger} \\ b_{-\mathbf{q}} \end{bmatrix}, \qquad (C1)$$

where $B_{\mathbf{q}}' = B_{\mathbf{q}} + SK_c$, $b^{\dagger}$ is the local spin deviation creation operator on the B sublattice, the sum extends over all wave vectors in the mBZ, and $A_{\mathbf{q}}$, $B_{\mathbf{q}}$ are the same as in Eq. (2). As can be seen, there are two flavors of operators. This 4×4 Hamiltonian matrix again can be brought to diagonal form using the following Bogoliubov basis transformation including two flavors of new spin-wave creation (annihilation) operators, corresponding to spin-wave modes polarized along **b** and **c**,

$$\begin{bmatrix} a_{\mathbf{q}} \\ b_{\mathbf{q}}^{\dagger} \\ a_{-\mathbf{q}}^{\dagger} \\ b_{-\mathbf{q}} \end{bmatrix} = \frac{1}{\sqrt{2}}\begin{bmatrix} u_{\mathbf{q}} & -v_{\mathbf{q}}' & -v_{\mathbf{q}} & -u_{\mathbf{q}}' \\ -v_{\mathbf{q}} & u_{\mathbf{q}}' & u_{\mathbf{q}} & v_{\mathbf{q}}' \\ -v_{\mathbf{q}} & -u_{\mathbf{q}}' & u_{\mathbf{q}} & -v_{\mathbf{q}}' \\ u_{\mathbf{q}} & v_{\mathbf{q}}' & -v_{\mathbf{q}} & u_{\mathbf{q}}' \end{bmatrix}\begin{bmatrix} \alpha_{\mathbf{q}} \\ \beta_{\mathbf{q}}^{\dagger} \\ \alpha_{-\mathbf{q}}^{\dagger} \\ \beta_{-\mathbf{q}} \end{bmatrix}. \qquad (C2)$$

The transformation thus yields two sets of terms, $u_{\mathbf{q}}$, $v_{\mathbf{q}}$, and $\omega_{\mathbf{q}}$ and $u_{\mathbf{q}}' = \cosh\theta_{\mathbf{q}}'$, $v_{\mathbf{q}}' = \sinh\theta_{\mathbf{q}}'$, and $\omega_{\mathbf{q}}'$, with

$$\tanh(2\theta_{\mathbf{q}}) = \frac{B_{\mathbf{q}}' - SK_c}{A_{\mathbf{q}}} = \frac{B_{\mathbf{q}}}{A_{\mathbf{q}}},$$

$$\tanh(2\theta_{\mathbf{q}}') = \frac{B_{\mathbf{q}}' + SK_c}{A_{\mathbf{q}}}$$

$$= -\frac{B_{\mathbf{q}+\boldsymbol{\tau}_{AF}}}{A_{\mathbf{q}+\boldsymbol{\tau}_{AF}}} = -\tanh(2\theta_{\mathbf{q}+\boldsymbol{\tau}_{AF}}), \qquad (C3)$$

and

$$\hbar\omega_{\mathbf{q}} = Z_c\sqrt{A_{\mathbf{q}}^2 - (B_{\mathbf{q}}' - SK_c)^2} = Z_c\sqrt{A_{\mathbf{q}}^2 - B_{\mathbf{q}}^2},$$

$$\hbar\omega_{\mathbf{q}}' = Z_c\sqrt{A_{\mathbf{q}}^2 - (B_{\mathbf{q}}' + SK_c)^2}$$

$$= Z_c\sqrt{A_{\mathbf{q}+\boldsymbol{\tau}_{AF}}^2 - B_{\mathbf{q}+\boldsymbol{\tau}_{AF}}^2} = \hbar\omega_{\mathbf{q}+\boldsymbol{\tau}_{AF}}. \qquad (C4)$$

Here we again use the fact that $2\boldsymbol{\tau}_{AF}$ is a reciprocal-lattice vector.

The correlations functions S^{bb} and S^{cc} follow as

$$S^{bb}(\mathbf{q}, \omega) = \frac{Z_d S}{2}|u_{\mathbf{q}} - v_{\mathbf{q}}|^2\delta(\hbar\omega - \hbar\omega_{\mathbf{q}}), \qquad (C5)$$

$$S^{cc}(\mathbf{q}, \omega) = \frac{Z_d S}{2}|u_{\mathbf{q}}' - v_{\mathbf{q}}'|^2\delta(\hbar\omega - \hbar\omega_{\mathbf{q}}')$$

$$= \frac{Z_d S}{2}|u_{\mathbf{q}+\boldsymbol{\tau}_{AF}} + v_{\mathbf{q}+\boldsymbol{\tau}_{AF}}|^2\delta(\hbar\omega + \hbar\omega_{\mathbf{q}+\boldsymbol{\tau}_{AF}}). \qquad (C6)$$

Using the relations between $\tanh(2\theta_{\mathbf{q}})$ and $\tanh(2\theta_{\mathbf{q}}')$ through the translation by $\boldsymbol{\tau}_{AF}$ from Appendix B, Eqs. (C5) and (C6) can be written as Eqs. (5) and (6), and thus yield the same results as the rotating frame method.

The longitudinal dynamical correlations take the form

$$S^{aa}(\mathbf{q}, \omega) = N(S - \Delta S)^2\delta(\hbar\omega)\delta(\mathbf{q} - \boldsymbol{\tau} - \boldsymbol{\tau}_{AF})$$

$$+ \frac{Z_{2M}}{2N}\sum_{\mathbf{q}_1,\mathbf{q}_2}f'(\mathbf{q}_1, \mathbf{q}_2)\delta(\hbar\omega - \hbar\omega_{\mathbf{q}_1} - \hbar\omega_{\mathbf{q}_2}')$$

$$\times \delta(\mathbf{q} - \mathbf{q}_1 - \mathbf{q}_2 - \boldsymbol{\tau}), \qquad (C7)$$

where $f'(\mathbf{q}_1, \mathbf{q}_2) = |v_{\mathbf{q}_1}u_{\mathbf{q}_2}' - u_{\mathbf{q}_1}v_{\mathbf{q}_2}'|^2$. Using the transformations relations, we find that

$$f'(\mathbf{q}_1, \mathbf{q}_2) = |v_{\mathbf{q}_1}u_{\mathbf{q}_2}' - u_{\mathbf{q}_1}v_{\mathbf{q}_2}'|^2$$

$$= |v_{\mathbf{q}_1}u_{\mathbf{q}_2+\boldsymbol{\tau}_{AF}} + u_{\mathbf{q}_1}v_{\mathbf{q}_2+\boldsymbol{\tau}_{AF}}|^2$$

$$= f(\mathbf{q}_1, \mathbf{q}_2 + \boldsymbol{\tau}_{AF}). \qquad (C8)$$

Thus, we can transform Eq. (C7) to yield Eq. (7). In the antiferromagnetic unit cell description, the two spin-wave modes appear mixed in the two-magnon scattering and applying the shift by $\boldsymbol{\tau}_{AF}$ effectively "decouples" the modes.

APPENDIX D: DZYALOSHINSKII-MORIYA INTERACTION

A finite Dzyaloshinskii-Moriya interaction (DMI) in a Néel SLAFM yields two nondegenerate spin-wave modes similar to the hard-axis anisotropy K_c. Contrary to a hard-axis anisotropy, DMI also yields a spin canting, which can be estimated from Eq. (3) in Ref. [26]. The reported spin canting of $0.1°$ implies a DMI of $\leqslant 0.1$ meV. Conversely, to establish the observed gap between the two spin-wave modes [20], for $K_c = 0$, numeric LSWT calculations [37] suggest a required DMI of ≈ 3.5 meV, yielding a spin canting of $\approx 3.5°$, which is $35\times$ larger than the reported value [26]. So, the effect from the DMI on the dynamics is much smaller than the effect from the K_c and is hence negligible.

[1] J. G. Bednorz and K. A. Müller, Possible high T_c superconductivity in the Ba-La-Cu-O system, Z. Phys. B: Condens. Matter **64**, 189 (1986).

[2] D. Li, K. Lee, B. Y. Wang, M. Osada, S. Crossley, H. R. Lee, Y. Cui, Y. Hikita, and H. Y. Hwang, Superconductivity in an infinite-layer nickelate, Nature (London) **572**, 624 (2019).

[3] T. Huberman, R. Coldea, R. A. Cowley, D. A. Tennant, R. L. Leheny, R. J. Christianson, and C. D. Frost, Two-magnon excitations observed by neutron scattering in the two-dimensional

spin-$\frac{5}{2}$ Heisenberg antiferromagnet Rb$_2$MnF$_4$, Phys. Rev. B **72**, 014413 (2005).

[4] R. Coldea, S. M. Hayden, G. Aeppli, T. G. Perring, C. D. Frost, T. E. Mason, S.-W. Cheong, and Z. Fisk, Spin Waves and Electronic Interactions in La$_2$CuO$_4$, Phys. Rev. Lett. **86**, 5377 (2001).

[5] N. S. Headings, S. M. Hayden, R. Coldea, and T. G. Perring, Anomalous High-Energy Spin Excitations in the High-T_c Superconductor-Parent Antiferromagnet La$_2$CuO$_4$, Phys. Rev. Lett. **105**, 247001 (2010).

[6] H. M. Rønnow, D. F. McMorrow, R. Coldea, A. Harrison, I. D. Youngson, T. G. Perring, G. Aeppli, O. Syljuåsen, K. Lefmann, and C. Rischel, Spin Dynamics of the 2D Spin $\frac{1}{2}$ Quantum Antiferromagnet Copper Deuteroformate Tetradeuterate (CFTD), Phys. Rev. Lett. **87**, 037202 (2001).

[7] B. Dalla Piazza, M. Mourigal, N. B. Christensen, G. J. Nilsen, P. Tregenna-Piggott, T. G. Perring, M. Enderle, D. F. McMorrow, D. A. Ivanov, and H. M. Rønnow, Fractional excitations in the square-lattice quantum antiferromagnet, Nat. Phys. **11**, 62 (2015).

[8] N. B. Christensen, H. M. Rønnow, D. F. McMorrow, A. Harrison, T. G. Perring, M. Enderle, R. Coldea, L. P. Regnault, and G. Aeppli, Quantum dynamics and entanglement of spins on a square lattice, Proc. Natl. Acad. Sci. **104**, 15264 (2007).

[9] N. Tsyrulin, T. Pardini, R. R. P. Singh, F. Xiao, P. Link, A. Schneidewind, A. Hiess, C. P. Landee, M. M. Turnbull, and M. Kenzelmann, Quantum Effects in a Weakly Frustrated $S = 1/2$ Two-Dimensional Heisenberg Antiferromagnet in an Applied Magnetic Field, Phys. Rev. Lett. **102**, 197201 (2009).

[10] N. Tsyrulin, F. Xiao, A. Schneidewind, P. Link, H. M. Rønnow, J. Gavilano, C. P. Landee, M. M. Turnbull, and M. Kenzelmann, Two-dimensional square-lattice $S = 1/2$ antiferromagnet Cu(pz)$_2$(ClO$_4$)$_2$, Phys. Rev. B **81**, 134409 (2010).

[11] C. H. Wang, M. D. Lumsden, R. S. Fishman, G. Ehlers, T. Hong, W. Tian, H. Cao, A. Podlesnyak, C. Dunmars, J. A. Schlueter, J. L. Manson, and A. D. Christianson, Magnetic properties of the $S = 1/2$ quasisquare lattice antiferromagnet CuF$_2$(H$_2$O)$_2$(pyz) (pyz=pyrazine) investigated by neutron scattering, Phys. Rev. B **86**, 064439 (2012).

[12] J. Zaanen, G. A. Sawatzky, and J. W. Allen, Band Gaps and Electronic Structure of Transition-Metal Compounds, Phys. Rev. Lett. **55**, 418 (1985).

[13] D. I. Khomskii, *Transition Metal Compounds* (Cambridge University Press, UK, 2015).

[14] X. L. Wang, C. Stassis, D. C. Johnston, T. C. Leung, J. Ye, B. N. Harmon, G. H. Lander, A. J. Schultz, C.-K. Loong, and J. M. Honig, The antiferromagnetic form factor of La$_2$NiO$_4$, J. Appl. Phys. **69**, 4860 (1991).

[15] X.-Li Wang, C. Stassis, D. C. Johnston, T. C. Leung, J. Ye, B. N. Harmon, G. H. Lander, A. J. Schultz, C.-K. Loong, and J. M. Honig, Neutron-diffraction study of the antiferromagnetic form factor of La$_2$NiO$_4$, Phys. Rev. B **45**, 5645 (1992).

[16] G. H. Lander, P. J. Brown, J. Spalek, and J. M. Honig, Structural and magnetization density studies of La$_2$NiO$_4$, Phys. Rev. B **40**, 4463 (1989).

[17] R. R. P. Singh, Thermodynamic parameters of the $T = 0$, spin-1/2 square-lattice Heisenberg antiferromagnet, Phys. Rev. B **39**, 9760 (1989).

[18] J. Rodriguez-Carvajal, M. T. Fernandez-Diaz, and J. L. Martinez, Neutron diffraction study on structural and magnetic properties of La$_2$NiO$_4$, J. Phys.: Condens. Matter **3**, 3215 (1991).

[19] G. Aeppli and D. J. Buttrey, Magnetic Correlations in La$_2$NiO$_{4+\delta}$, Phys. Rev. Lett. **61**, 203 (1988).

[20] K. Nakajima, K. Yamada, S. Hosoya, T. Omata, and Y. Endoh, Spin-Wave Excitations in Two Dimensional Antiferromagnet of Stoichiometric La$_2$NiO$_4$, J. Phys. Soc. Jpn. **62**, 4438 (1993).

[21] G. Fabbris, D. Meyers, L. Xu, V. M. Katukuri, L. Hozoi, X. Liu, Z.-Y. Chen, J. Okamoto, T. Schmitt, A. Uldry, B. Delley, G. D. Gu, D. Prabhakaran, A. T. Boothroyd, J. van den Brink, D. J. Huang, and M. P. M. Dean, Doping Dependence of Collective Spin and Orbital Excitations in the Spin-1 Quantum Antiferromagnet La$_{2-x}$Sr$_x$NiO$_4$ Observed by X Rays, Phys. Rev. Lett. **118**, 156402 (2017).

[22] D. J. Buttrey, J. M. Honig, and C. N. R. Rao, Magnetic properties of quasi-two-dimensional La$_2$NiO$_4$, J. Solid State Chem. **64**, 287 (1986).

[23] R. A. Ewings, J. R. Stewart, T. G. Perring, R. I. Bewley, M. D. Le, D. Raspino, D. E. Pooley, G. Škoro, S. P. Waller, D. Zacek, C. A. Smith, and R. C. Riehl-Shaw, Upgrade to the MAPS neutron time-of-flight chopper spectrometer, Rev. Sci. Instrum. **90**, 035110 (2019).

[24] S. M. Hayden and A. T. Boothroyd, The search for long range exchange interactions in the $S = 1$ square lattice antiferromagnet La$_2$NiO$_4$, STFC ISIS Neutron and Muon Source, https://doi.org/10.5286/isis.e.24078704.

[25] G. E. Granroth, A. I. Kolesnikov, T. E. Sherline, J. P. Clancy, K. A. Ross, J. P. C. Ruff, B. D. Gaulin, and S. E. Nagler, SEQUOIA: A newly operating chopper spectrometer at the SNS, J. Phys.: Conf. Ser. **251**, 012058 (2010).

[26] K. Yamada, T. Omata, K. Nakajima, S. Hosoya, T. Sumida, and Y. Endoh, Magnetic structure and weak ferromagnetism of La$_2$NiO$_{4+\delta}$, Physica C: Superconductivity **191**, 15 (1992).

[27] R. A. Ewings, A. Buts, M. D. Le, J. van Duijn, I. Bustinduy, and T. G. Perring, Horace: Software for the analysis of data from single crystal spectroscopy experiments at time-of-flight neutron instruments, Nucl. Instrum. Methods Phys. Res., Sect. A **834**, 132 (2016).

[28] See Supplemental Material at http://link.aps.org/supplemental/10.1103/PhysRevResearch.5.033113 for the data shown in Fig. 4(a).

[29] C. M. Canali and M. Wallin, Spin-spin correlation functions for the square-lattice Heisenberg antiferromagnet at zero temperature, Phys. Rev. B **48**, 3264 (1993).

[30] C. M. Canali, S. M. Girvin, and M. Wallin, Spin-wave velocity renormalization in the two-dimensional Heisenberg antiferromagnet at zero temperature, Phys. Rev. B **45**, 10131 (1992).

[31] M. Roger and J. M. Delrieu, Cyclic four-spin exchange on a two-dimensional square lattice: Possible applications in high-T_c superconductors, Phys. Rev. B **39**, 2299 (1989).

[32] A. Chubukov, E. Gagliano, and C. Balseiro, Phase diagram of the frustrated spin-1/2 Heisenberg antiferromagnet with cyclic-exchange interaction, Phys. Rev. B **45**, 7889 (1992).

[33] W. Nolting and A. Ramakanth, *Quantum Theory of Magnetism* (Springer-Verlag, Berlin, 2009).

[34] W. Marshall and S. W. Lovesey, *Theory of Thermal Neutron Scattering* (Oxford University Press, UK, 1971).

[35] J. Oitmaa and C. J. Hamer, $S = 1$ bilinear biquadratic spin model on the square lattice: A series expansion study, Phys. Rev. B **87**, 224431 (2013).

[36] N. Papanicolaou, Unusual phases in quantum spin-1 systems, Nucl. Phys. B **305**, 367 (1988).

[37] T. A. Tóth, A. M. Läuchli, F. Mila, and K. Penc, Competition between two- and three-sublattice ordering for $S = 1$ spins on the square lattice, Phys. Rev. B **85**, 140403(R) (2012).

[38] S. Toth and B. Lake, Linear spin wave theory for single-Q incommensurate magnetic structures, J. Phys.: Condens. Matter **27**, 166002 (2015).

[39] A. H. MacDonald, S. M. Girvin, and D. Yoshioka, $\frac{t}{U}$ expansion for the Hubbard model, Phys. Rev. B **37**, 9753 (1988).

[40] A. H. MacDonald, S. M. Girvin, and D. Yoshioka, Reply to "Comment on 't/U expansion for the Hubbard model' ", Phys. Rev. B **41**, 2565 (1990).

[41] D. J. Klein and W. A. Seitz, Perturbation Expansion of the Linear Hubbard Model, Phys. Rev. B **8**, 2236 (1973).

[42] T. Kato, On the Convergence of the Perturbation Method. I, Prog. Theor. Phys. **4**, 514 (1949).

[43] J.-ichi Igarashi, $1/S$ expansion for thermodynamic quantities in a two-dimensional Heisenberg antiferromagnet at zero temperature, Phys. Rev. B **46**, 10763 (1992).

[44] R. M. White, M. Sparks, and I. Ortenburger, Diagonalization of the Antiferromagnetic Magnon-Phonon Interaction, Phys. Rev. **139**, A450 (1965).

[45] I. U. Heilmann, J. K. Kjems, Y. Endoh, G. F. Reiter, G. Shirane, and R. J. Birgeneau, One- and two-magnon excitations in a one-dimensional antiferromagnet in a magnetic field, Phys. Rev. B **24**, 3939 (1981).

[46] R. A. Ewings, T. G. Perring, R. I. Bewley, T. Guidi, M. J. Pitcher, D. R. Parker, S. J. Clarke, and A. T. Boothroyd, High-energy spin excitations in $BaFe_2As_2$ observed by inelastic neutron scattering, Phys. Rev. B **78**, 220501(R) (2008).

[47] J. Lorenzana, G. Seibold, and R. Coldea, Sum rules and missing spectral weight in magnetic neutron scattering in the cuprates, Phys. Rev. B **72**, 224511 (2005).

[48] R. Coldea, D. A. Tennant, and Z. Tylczynski, Extended scattering continua characteristic of spin fractionalization in the two-dimensional frustrated quantum magnet Cs_2CuCl_4 observed by neutron scattering, Phys. Rev. B **68**, 134424 (2003).

[49] R. J. Weiss and A. J. Freeman, X-ray and neutron scattering from electrons in a crystalline field and the determination of outer electron configurations in iron and nickel, J. Phys. Chem. Solids **10**, 147 (1959).

[50] E. Clementi and C. Roetti, Roothaan-Hartree-Fock atomic wave functions: Basis functions and their coefficients for ground and certain excited states of neutral and ionized atoms, $Z \geqslant 54$, At. Data Nucl. Data Tables **14**, 177 (1974).

[51] J. P. Desclaux and A. J. Freeman, Dirac-Fock studies of some electronic properties of actinide ions, J. Magn. Magn. Mater. **8**, 119 (1978).

[52] A. J. Freeman and J. P. Desclaux, Dirac-Fock studies of some electronic properties of rare-earth ions, J. Magn. Magn. Mater. **12**, 11 (1979).

[53] I. S. Anderson, P. J. Brown, J. M. Carpenter, G. Lander, R. Pynn, J. M. Rowe, O. Schärpf, V. F. Sears, and B. T. M. Willis, Neutron techniques, in *International Tables for Crystallography*, edited by E. Prince (International Union of Crystallography, Chester, UK, 2006), pp. 430–487.

[54] M. Takahashi, Half-filled Hubbard model at low temperature, J. Phys. C **10**, 1289 (1977).

[55] P. Babkevich, D. Prabhakaran, C. D. Frost, and A. T. Boothroyd, Magnetic spectrum of the two-dimensional antiferromagnet La_2CoO_4 studied by inelastic neutron scattering, Phys. Rev. B **82**, 184425 (2010).

[56] R. Verresen, F. Pollmann, and R. Moessner, Quantum dynamics of the square-lattice Heisenberg model, Phys. Rev. B **98**, 155102 (2018).

[57] W. Koshibae, Y. Ohta, and S. Maekawa, Theory of Dzyaloshinski-Moriya antiferromagnetism in distorted CuO_2 and NiO_2 planes, Phys. Rev. B **50**, 3767 (1994).

[58] J. F. Annett, R. M. Martin, A. K. McMahan, and S. Satpathy, Electronic Hamiltonian and antiferromagnetic interactions in La_2CuO_4, Phys. Rev. B **40**, 2620 (1989).

[59] R. R. P. Singh and M. P. Gelfand, Spin-wave excitation spectra and spectral weights in square lattice antiferromagnets, Phys. Rev. B **52**, R15695(R) (1995).

[60] W. Zheng, J. Oitmaa, and C. J. Hamer, Series studies of the spin-$\frac{1}{2}$ Heisenberg antiferromagnet at $T = 0$: Magnon dispersion and structure factors, Phys. Rev. B **71**, 184440 (2005).

[61] A. W. Sandvik and R. R. P. Singh, High-Energy Magnon Dispersion and Multimagnon Continuum in the Two-Dimensional Heisenberg Antiferromagnet, Phys. Rev. Lett. **86**, 528 (2001).

[62] H. Shao, Y. Qi Qin, S. Capponi, S. Chesi, Z. Y. Meng, and A. W. Sandvik, Nearly Deconfined Spinon Excitations in the Square-Lattice Spin-1/2 Heisenberg Antiferromagnet, Phys. Rev. X **7**, 041072 (2017).

[63] A. Lüscher and A. M. Läuchli, Exact diagonalization study of the antiferromagnetic spin-1/2 Heisenberg model on the square lattice in a magnetic field, Phys. Rev. B **79**, 195102 (2009).

[64] M. Powalski, K. P. Schmidt, and G. S. Uhrig, Mutually attracting spin waves in the square-lattice quantum antiferromagnet, SciPost Phys. **4**, 001 (2018).

[65] M. Powalski, G. S. Uhrig, and K. P. Schmidt, Roton Minimum as a Fingerprint of Magnon-Higgs Scattering in Ordered Quantum Antiferromagnets, Phys. Rev. Lett. **115**, 207202 (2015).

[66] A. T. Boothroyd, *Principles of Neutron Scattering from Condensed Matter* (Oxford University Press, UK, 2020).